Propagation of interplanetary (IP) shocks near the Earth

Masatoshi Yamauchi[1,*], Yoshihiro Yokoyama[2,*], Tsubasa Kotani[3], and Jügen Matzka[4]

[1]Swedish Institute of Space Physics, Kiruna, Sweden
[2]UiT, Arctic University of Norway, Tromsø, Norway
[3]Data Analysis Center for Geomagnetism and Space Magnetism, Graduate School of Science, Kyoto University, Kyoto, Japan
[4]GFZ Helmholtz Centre for Geosciences, Potsdam, Germany
[*]This author contributed equally to this work.

Correspondence: M.Yamauchi (M.Yamauchi@irf.se)

Abstract. Solar wind values monitored at the Sun-Earth L1 point have been used to estimate the Earth-arrival time of interplanetary (IP) shocks associated with coronal mass ejections (CMEs) and co-rotating interaction regions (CIRs). In standard estimates, including NASA/OMNI database, the radial propagation speed of the IP shock is assumed to be the same as the measured solar wind (proton) speed after the shock, although these speeds are known to be different in both the shock theory and CME observations. To diagnose the actual error in the arrival time of the IP shocks, we statistically compared the radial propagation speed of the IP shock with the measured solar wind speed at L1. The propagation speed is obtained from the time-of-propagation between the IP shock passage at the L1 monitoring point and the geomagnetic sudden commencement (SC) at the Earth. As the L1 monitoring point, we use three locations: two are the spacecraft (SOHO and ACE) locations, and the other is the estimated IP shock passage point upstream of the Earth at $Y = 0$ in Geocentric Solar Ecliptic (GSE) coordinate, calculated from timings and locations of the IP shock passage at both spacecraft. In statistics, we limited to the IP shocks with a clear geomagnetic SC signature and with velocity profiles consistent between SOHO and ACE. During 1998-2022, 375 IP shocks satisfied such conditions. For the solar wind speed ($V_{\rm SW}$), the highest value during 15 min after the IP shock passage observed by the selected spacecraft (SOHO or ACE) was used. We found the following tendencies. (1) As expected from the shock theory, arrival time of the IP shock to the Earth (represented by the geomagnetic SC) is earlier than the predicted arrival time of the shocked solar wind by $0-10$ min. (2) The speed difference between the shock propagation and $V_{\rm SW}$ is about $+10\%$, which is in the same order of magnitude as that expected from the 1D shock model with typical solar wind parameters across the shock. (3) The distribution of the velocity ratio between the shock propagation and the solar wind is, although statistics is not sufficient, slightly asymmetric toward higher ratio (faster propagation) with respect to the center of the distribution, which is already 1.1 instead of unity.

1 Introduction

In solar-terrestrial physics including the relevant magnetospheric physics and space weather predictions, upstream monitoring of the solar wind parameters such as the velocity, density, and the interplanetary magnetic field (IMF) is essential. The upstream measurements of these values have been continuously made by monitoring spacecraft at the Sun-Earth Lagrange L1 region for

nearly three decades by Wind (Oglivie et al., 1995), SOHO (McComas et al., 1998) and ACE (Ipavich, 1998), and one decade by DSCOVR. With solar wind velocity and distance between these spacecraft and the Earth, one can roughly estimate the arrival time of the coronal mass ejection (CME) and other large changes in these parameters, such as interplanetary (IP) shocks and large IMF changes.

In these estimates of the arrival time, the earthward propagation speed of the CME and other IP shocks along the Geocentric Solar Ecliptic (GSE) coordinate $-X_{\rm GSE}$ direction is normally assumed to be the same as the solar wind speed (anti-sunward proton speed) after the shock measured at L1 (King and Papitashvili, 2026). However, the propagation speed of the IP shocks is known to be different from the solar wind speed in both the shock theory and CME observations.

For observation near the Sun, the CME front identified by SOHO LASCO imager sometimes propagates at velocity >1000 km/s, being much faster than the solar wind velocity measured at L1 (e.g., Manoharan et al., 2001; Yashiro et al., 2004; Tokumaru et al., 2006; Gonzalez-Esparza and Aguilar-Rodriguez, 2009; Gopalswamy, 2009). Although the CME propagation is decelerated while the solar wind is accelerated with distance from the Sun, the IP shocks propagate faster than the solar wind even near the Earth.

In 1D shock models, the conservation of the mass flux across the shock in the shock-rest frame (Rankine-Hugoniot relation) requires that the higher-density side (solar wind after the IP shock passage for forward shock) should have lower relative velocity to the shock. This condition can be achieved only if the shock speed is higher than the solar wind speed (see Fig. A1 in Appendix A for this textbook type relation).

Theoretically, the shock propagation speed should be able to be derived from the measured changes in velocity and density. However, the observation of density, particularly its large increase, is often erroneous right after the IP shocks, causing such a calculated result unreliable (cf. Fig. A1e in Appendix A). This is one of the reasons why the solar wind speed is used for predicting the arrival time of the IP shocks at the Earth. Furthermore, the actual IP shocks are not as ideal as simple models, and it is wise to avoid using density information in automated prediction of the propagation speed (an example is shown later).

The time difference comes also from the other reasons. If the IP shock front surface ("phase plane") is oblique like the sector boundary, we expect both earlier or delayed arrival of the IP shock to the Earth compared to the predicted arrival time using L1 monitor value, because the location of the monitor spacecraft (SOHO, ACE, and DSCOVR) is offset from the Sun-Earth line (Richardson and Paularena, 1998; Collier et al., 1998). This "oblique" effect can be significant because the GSE Y-Z location of the L1 monitor is normally at a large distance (up to $\sim 3\times10^5$ km for ACE (https://izw1.caltech.edu/ACE/ASC/DATA/browse-html/y_z_plot.gif) and up to $\sim 7\times10^5$ km for SOHO (https://soho.nascom.nasa.gov/about/orbit.html)) away from the Sun-Earth line in the huge L1 region. Fortunately, both SOHO and ACE take nearly symmetric orbits with respect to the Sun-Earth line (i.e., in the GSE Y-Z direction). Therefore, the statistical average of the actual arrival time is expected to converge to the expected arrival time, unlike the time difference coming from the difference in speeds.

Another possibility is when the IP shock propagates "obliquely" in the GSE Y-Z direction, like the flank side of CMEs or when a fast stream approaches the equatorial region from north or south. In such cases, the $X_{\rm GSE}$ component of the shock front's phase velocity will be quite different from the solar wind velocity (cf. Figs. A1c and A1d in Appendix A). Fortunately,

we again expect both earlier or delayed arrival of the IP shock to the Earth compared to the prediction using the solar wind speed values, and the same argument of the symmetricity above applies to the statistic.

Since the arrival time of the IP shocks to the Earth is one of the essential information in understanding the solar wind-magnetosphere interaction including the space weather prediction, it is quite important to examine the degree of difference between the radial propagation speed of IP shocks (particularly of CMEs) and the speed of the solar wind near the Earth. This type of difference has been reported for the transit time of the IMF changes (e.g., Collier et al., 1998; Milan et al., 2022), but less well studied for the IP shocks (e.g., Paularena et al., 1998, 1999). Particularly, no statistical study on the difference in the speed (between the IP shock propagation and solar wind) near the Earth was made, although the statistical study is mandatory from the above reasons.

The purpose of this paper is to statistically examine the velocity difference between the IP shock propagation and solar wind speed (accordingly, the difference in the arrival time to the Earth) using the solar wind data from the L1 monitoring spacecraft (both SOHO and ACE) and the geomagnetic data. From solar wind data, we obtained the timing of the IP shock passage ($T_{\rm soho}$ for SOHO and $T_{\rm ace}$ for ACE) at the spacecraft location and the solar wind speed ($V_{\rm SW}$) after the IP shock passage, whereas we used geomagnetic data to determine the timing of the geomagnetic sudden commencement (SC) as the proxy of the arrival time of the IP shock to the Earth ($T_{\rm SC}$). We do not use density data that can be underestimated after the shock due to saturation. Decades of L1 monitoring by SOHO (since 1996) and ACE (since 1997) allows us to take statistics on the difference in speed between the IP shock propagation and the solar wind, using a sufficient number of IP shocks that are identified in both spacecraft with clear geomagnetic SC signatures.

2 Data and Method

Located at the Sun-Earth L1 point, which is about 1.5×10^6 km upstream of the Earth, SOHO and ACE monitor the upstream solar wind. The time resolution of the solar wind data that we used is about 30s for SOHO and 1 min for ACE, and that for the timing of the geomagnetic SC ($T_{\rm SC}$) is also 1 min. Technical descriptions of the solar wind monitoring instruments are found in Ipavich (1998) for SOHO and McComas et al. (1998) for ACE. Although we conventionally call L1 "point", all L1 monitoring spacecraft take the semi-periodical halo orbit around L1, which covers much larger areas than the size of the Earth (radius of 0.07×10^5 km): the distance from the L1 point in the GSE Y-Z plane can be up to 7×10^5 km for SOHO (https://soho.nascom.nasa.gov/about/orbit.html) and 3×10^5 km for ACE (https://izw1.caltech.edu/ACE/ASC/DATA/browse-html/y_z_plot.gif).

We start from the IP shock list of SOHO (https://space.umd.edu/pm/figs/history.html) and manually examined the velocity profile during 1996-2022 for SOHO and 1998-2022 for ACE. The solar wind data and spacecraft locations are obtained from the NASA Omniweb site (https://cdaweb.gsfc.nasa.gov/). We examined these data to obtain both the timing of the IP shock and the solar wind velocity. We limit the IP shocks to those that are not contaminated by high-speed periods before the IP shock. Among them, we selected those that also caused a clear geomagnetic SC signature, which indicates the arrival of the IP shock to the Earth. All these filtering are done by manually.

The geomagnetic SC is a sudden increase in the horizontal (H) component in the dayside stations that propagates quickly to the nightside (e.g., Araki, 1977; 1994). Since the propagation time of the SC signature from the magnetopause to the Earth, which is 1-3 min, is about the same as the travelling time of the solar wind from the magnetopause to the Earth's terminator, we can safely use the onset time of the geomagnetic SC ($T_{\rm SC}$) as a proxy of arrival time of the IP shock to the Earth (e.g., Earth's terminator).

In this method of estimating the arrival time of the IP shock, the geomagnetic variation is sometimes contaminated by on-going geomagnetic activities (this can also be examined by the geomagnetic AE index). Therefore, we also limit to the cases when the geomagnetic SC is clearly identified in SYM-H index (e.g., Nanjo et al., 2025), which is provided by WDC for geomagnetism, Kyoto (https://wdc.kugi.kyoto-u.ac.jp/aeasy/index.html). This gives us 438 examples out of more than 650 IP shocks in the list. To confirm our list of the geomagnetic SC, we also used the SC list provided by the Ebre Observatory (https://www.obsebre.es/en/variations/rapid), in which the magnetometer data from five longitudinally distributed low-latitude stations are used to identify the geomagnetic SC.

2.1 Example

Fig. 1 shows an example of such IP shocks. Figs. 1a and 1b show that a sudden sharp increase in the proton speed (thick black line) and density (thin blue line) occurred simultaneously for both SOHO at 13:35 UT (Fig. 1a) and ACE at 13:30 UT (Fig. 1b) on 2006-01-01. Also, the total IMF strength (dashed red line) observed by ACE suddenly increased simultaneously at 13:30 UT. Since the IP shock timing was identified as a sudden increase in dynamic pressure, the above timing corresponds to the IP shock timing passing through SOHO and ACE, respectively. Fig. 1c shows that SYM-H suddenly increased at 14:05 UT as an isolated geomagnetic SC during a quiet period without any contamination from any magnetospheric activities (as seen from AU and AL indices).

Let us estimate the propagation speed of the IP shock in the $-X_{\rm GSE}$ direction. From the above timings, travel time of the IP shock is estimated as $dt_{\rm soho} = 30 \pm 1$ min for SOHO-Earth propagation and $dt_{\rm ace} = 35 \pm 1$ min for ACE-Earth propagation. We consider the following three cases.

(a) If the shock normal (phase plane normal) points the $-X_{\rm GSE}$ direction, the $X_{\rm soho}$ distance of 1.263×10^6 km means about $\sim 700 \pm 30$ km/s, and $X_{\rm ace} = 1.440 \times 10^6$ km means about $\sim 690 \pm 20$ km/s. Both values are consistent with each other, but much faster than the measured solar wind speed. To check this, we also estimated the propagation speed from the $X_{\rm GSE}$ location of ACE to the $X_{\rm GSE}$ location of SOHO (i.e., 1.77×10^5 km) and the 5 ± 1 min time lag between these two $X_{\rm GSE}$ locations. This gives us $\sim 590 \pm 150$ km/s along $-X_{\rm GSE}$ direction, which is within the consistent range with the above values.

We next consider when the shock normal is tilted from the GSE $-X$ direction. Since we have only two spacecraft, we have to assume the tilt direction within one 2D plane. Since the tilt direction most likely reflect the major offset direction of the source CME on the solar surface, which is distributed all longitudes but only in a limited latitude range near the equator, the tilt direction is generally expected in the X–Y direction rather than in the X–Z direction.

(b) If the shock front is tilted by 45° in the GSE X–Y direction, we have to take into consideration of the GSE Y location of the spacecraft (GSE $Y_{\rm soho} = 4.69 \times 10^5$ km for SOHO and $Y_{\rm ace} = -2.47 \times 10^5$ km for ACE). Projecting these locations to GSE

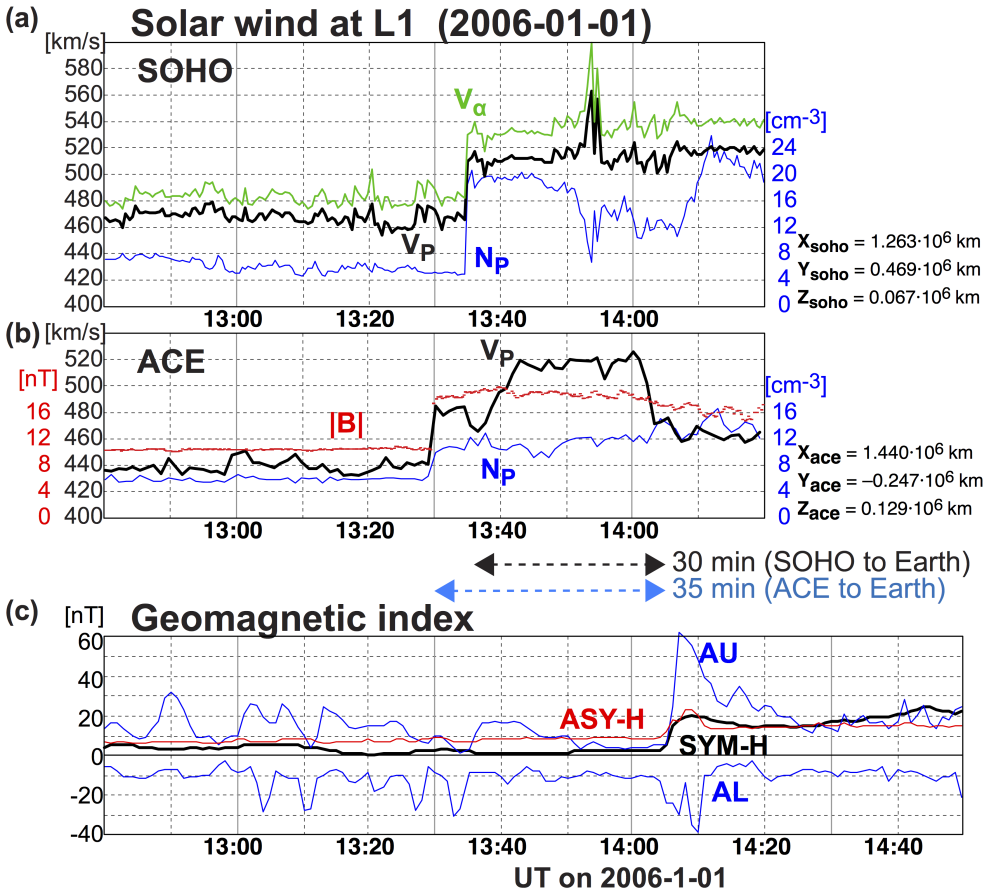

Figure 1. Solar wind data observed by (a) SOHO and (b) ACE for the IP shock event on 2006-01-01. The proton speed, proton density, and the IMF intensity are plotted by thick black lines, thin blue lines, and a thin red line, respectively. As a reference, speed of the alpha particle is also plotted by a green line in the top panel.. The IP shock is identified as sudden simultaneous intensification of the density and velocity for both SOHO (13:35 UT) and ACE (13:30 UT). The IMF total field measured by ACE also shows sudden intensification at the same timing (13:30 UT). (c) Geomagnetic indices SYM-H (thick black lines), ASY-H (thin red line), AU and AL (both thin blue lines) for the same IP shock. Sudden increase of SYM-H (and ASY-H and AU) is observed at 14:05 UT.

$Y = 0$ along the shock front, the X distance to the IP shock on the Sun-Earth line is estimated as 1.732×10^6 km at 13:35 UT for SOHO and as 1.193×10^6 km at 13:30 UT for ACE. These values give about $\sim 960 \pm 30$ km/s and $\sim 570 \pm 20$ km/s (both in the $-X_{\rm GSE}$ direction) from the SOHO-Earth timing and ACE-Earth timings, respectively. Meanwhile, the inter-spacecraft time lag of 5 ± 1 min also means a backward propagation with -1800 ± 450 km/s. All estimates of the propagation velocity (SOHO to the Earth, ACE to the Earth, and ACE to SOHO) contradict each other.

(c) The tilt angle of the IP shock normal in the GSE X–Y direction (θ) can be estimated by assuming that the IP shock front is 2D plane tilted in the GSE X–Y direction only (1D-shock). Under these assumptions, propagation speed of the IP

shock ($V_{\rm triangle}$), with oblique shock front that is tilted by θ, from the upstream point ($Y_{\rm GSE}$=0) to the Earth becomes the same between using the projected SOHO location to the upstream point and using the projected ACE location to the upstream point:

$$V_{\rm triangle} = [X_{\rm soho} + (Y_{\rm soho} \cdot \tan\theta)]/dt_{\rm soho} \quad (1)$$
$$= [X_{\rm ace} + (Y_{\rm ace} \cdot \tan\theta)]/dt_{\rm ace}$$

or

$$\tan\theta = -\frac{(X_{\rm soho}/dt_{\rm soho}) - (X_{\rm ace}/dt_{\rm ace})}{(Y_{\rm soho}/dt_{\rm soho}) - (Y_{\rm ace}/dt_{\rm ace})} \quad (2)$$

For the Fig. 1 event, this relation gives an estimate of $\theta = -2^\circ \pm 11^\circ$, and propagation speed of IP shock as 690 ± 70 km/s. This agrees with the case (a) estimate above.

As reference, we also estimated the optimum tilt angle in the X–Z direction by assuming uniform configuration in the Y direction. The estimated tilt angle θ_Z is $33^\circ \pm 40^\circ$ (velocity 730 ± 100 km/s). Here, the large error bar comes from small relative location of the spacecraft in the Z direction, which forced us to extrapolate in the Z direction instead of interpolating in the Y direction.

From (a)–(c), we can safely assume that the shock normal points nearly along the $-X_{\rm GSE}$ direction, with the IP propagation speed of ~ 690 km/s (all estimates include a common range of $670 - 710$ km/s). This is much higher than the maximum solar wind speed of 519 km/s (same value for both SOHO and ACE) observed within 15 min after the IP shock passage. The duration of 15 min is sufficient for not missing the real peak value of fluctuating speed (or possible underestimation of the speed due to the instrument saturation) while it is short enough excluding independent velocity increase afterward, according to our manual examination of all the velocity plots of IP shock passages (in the same format as Fig. 1).

The derived IP shock propagation speed is even much faster than the theoretical propagation speed in a simple 1D shock model (cf. Appendix A). In the SOHO observation, the density jump across the IP shock passage is about 4 times, whereas the speed changed from 470 km/s to 520 km/s. These values lead to an estimate of 540 km/s as the propagation speed in the simple 1D shock model. On the other hand, the density jump across the shock observed by ACE is only double, i.e., much smaller than the SOHO observation, whereas the solar wind speed jumped from 440 km/s to 520 km/s, i.e., much larger than the SOHO observation. Accordingly, the estimated propagation speed in the same 1D shock model is 600 km/s.

The difference in the jump across the shock between the ACE observation and the SOHO observation might come from the instrumental difference (e.g., different saturation level) although it might reflect non-uniformity of the shock. Generally, density measurements are less reliable than the velocity measurements during high-flux events such as CME. A saturation of measurement after the shock passage causes underestimation of the density jump, which may result in overestimation of theoretical shock propagation speed (see Appendix A for more explanation). Even if the observation is real, these theoretical propagation speeds are still much lower than the observed propagation speed (690 ± 20 km/s). This example enforces the usefulness of statistical examination of the IP shock propagation speed against the solar wind speed, both of which are direct products of the most reliable measured values rather than theoretical estimates using less reliable measurements and extra assumptions.

Next, we estimate the travel time of the IP shock from SOHO or ACE to the Earth, using the solar wind (proton) velocity right after the shock. We take the highest value of the proton speed during 15 min after the shock detection, which is 519 km/s for both SOHO and ACE. Here, we assume the shock normal (phase plane normal) points nearly in the $-X_{\rm GSE}$ direction based on the above discussion (a)-(c).

The velocity value of 519 km/s predicts a travel time of 41 min from SOHO (GSE $X_{\rm soho} = 1.263 \times 10^6$ km) to the Earth and 46 min from ACE (GSE $X_{\rm ace} = 1.440 \times 10^6$ km) to the Earth. If we take these values as the shock propagation speed, the predicted arrival time of the same solar wind to the Earth is at 14:16 UT for both SOHO and ACE. If we take the value of 540 km/s (1D shock model applied to SOHO data, see above), the travel time reduces, but only by 2 min with a predicted arrival time of 14:14 UT. Even if we use the most likely overestimated value for ACE, the predicted arrival time is 14:10 UT, which is 5 minutes after the geomagnetic SC. By definition, the predicted arrival time using $V_{\rm triangle}$ is the same as the geomagnetic SC.

In summary, the anti-sunward propagation of the IP shock propagation on the 2006-01-01 event, which is estimated as ~ 690 km/s, is much faster than the solar wind (~ 520 km/s) or theoretical 1D shock propagation (~ 540 km/s). Accordingly, the actual IP shock arrived about 10 min earlier than the predicted arrival time based on the post-shock solar wind value ($520 - 540$ km/s).

2.2 Statistical method

We take statistics of two parameters. The first parameter is the time difference Δt between the expected arrival time of the shock-related solar wind and actual arrival time represented by the geomagnetic SC ($T_{\rm SC}$) detected in SYM-H. Positive Δt means earlier $T_{\rm SC}$ than the expected arrival of the solar wind. For the solar wind speed, we took the highest value during 15 min after the IP shock passage (cf. explanation at Fig. 1).

The second parameter is the estimated propagation speed of the IP shock in the $-X_{\rm GSE}$ direction. We use two methods that correspond to the case (a) and case (c) in the previous subsection (Sect. 2.1): (a) $V_{\rm timing}$ that is derived from the timing of the IP shock detection by one spacecraft ($T_{\rm soho}$ for SOHO or $T_{\rm ace}$ for ACE) and its $X_{\rm GSE}$ location by assuming that the shock normal points in the $-X_{\rm GSE}$ direction; (c) $V_{\rm triangle}$ that is derived from Eqs. (1) and (2) using both spacecraft assuming a tilt angle θ in the GSE X–Y. The derived propagation speed is compared with the post-shock solar wind speed $V_{\rm SW}$.

Fig. 2 shows the distribution of Δt: left panel (a) shows a scatter plot of Δt against the predicted travel time of the shock-related solar wind (from SOHO to the Earth) in the $X_{\rm GSE}$ direction; and right panel (b) shows the number of IP shocks at different Δt. Different colors in Fig. 2 (dark blue, light blue, and orange) represent different clearness of the SC signature (see the figure caption).

Fig. 2 includes IP shocks that are quite non-uniform in the GSE Y-Z direction. In fact, the velocity profile and particularly the density profile are often different between SOHO and ACE. Although the SOHO–ACE density differences might be attributed to the different measurement methods of the solar wind protons between SOHO and ACE (ACE generally has a lower saturation level than SOHO), the inter-spacecraft difference in the velocity profile mainly comes from the non-uniform structure of the

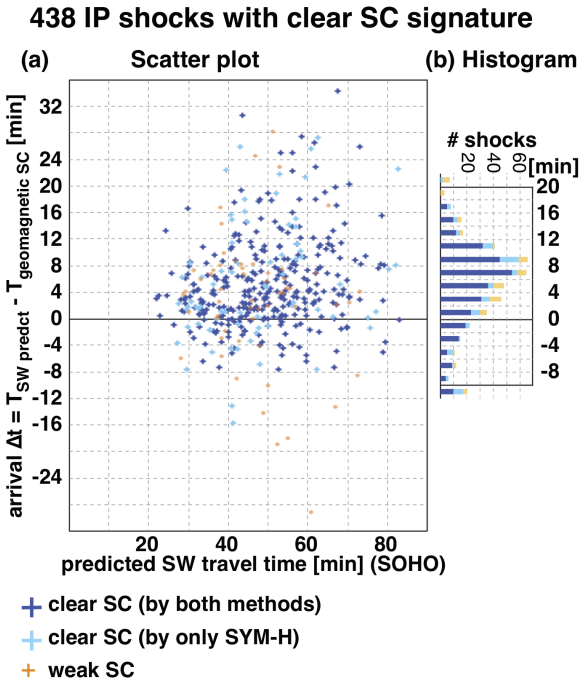

Figure 2. (a) Scatter plot of Δt against the predicted travel time in the $-X_{\rm GSE}$ direction (from SOHO to the Earth) for 438 IP shocks in which the IP shock and geomagnetic sudden commencement (SC) are one-to-one connected. Positive Δt means that the actual arrival of the IP shock to the Earth is earlier than the predicted arrival time using the solar wind speed measured by SOHO. The data are classified into three types in terms of clearness of the SC signature: dark blue, light blue, and orange represent those when the SC is clearly identified in the SYM-H index while it is also found in the SC list at Ebre Observatory (https://www.obsebre.es/en/variations/rapid), only in the SYM-H index, and only with weak or unclear SC signatures (e.g., amplitude less than 10 nT in SYM-H index or signature during some on-going activity), respectively. (b) Histogram of the time difference Δt, which is the same as the integration of panel (a) over all the travel time. The same colors are used for the sub-classified types.

IP shock because the location difference can be as large as 3×10^5 km in the $X_{\rm GSE}$ direction and 7×10^5 km in the GSE Y-Z direction. This is sufficiently large in detecting the non-uniform structure of the IP shock in the GSE Y-Z direction.

In this paper, we limit to cases when the velocity profiles are consistent between SOHO and ACE with a clear IP shock signature (e.g., the velocity is relatively stable before the IP shock as mentioned above), according to our manual examination of the velocity profiles. This gives us 375 "consistent" examples during 1998-2022, for which we can assume that the spacecraft detected the same IP shock.

Since the purpose is to obtain the difference between the shock propagation speed and the solar wind speed, we further select ideal ones from these "consistent" examples: those with the shock normal most likely pointing more or less in the $-X_{\rm GSE}$ direction, as illustrated with red and orange empty arrows in Fig. 3a. For such selection, a small tilt angle (θ) derived

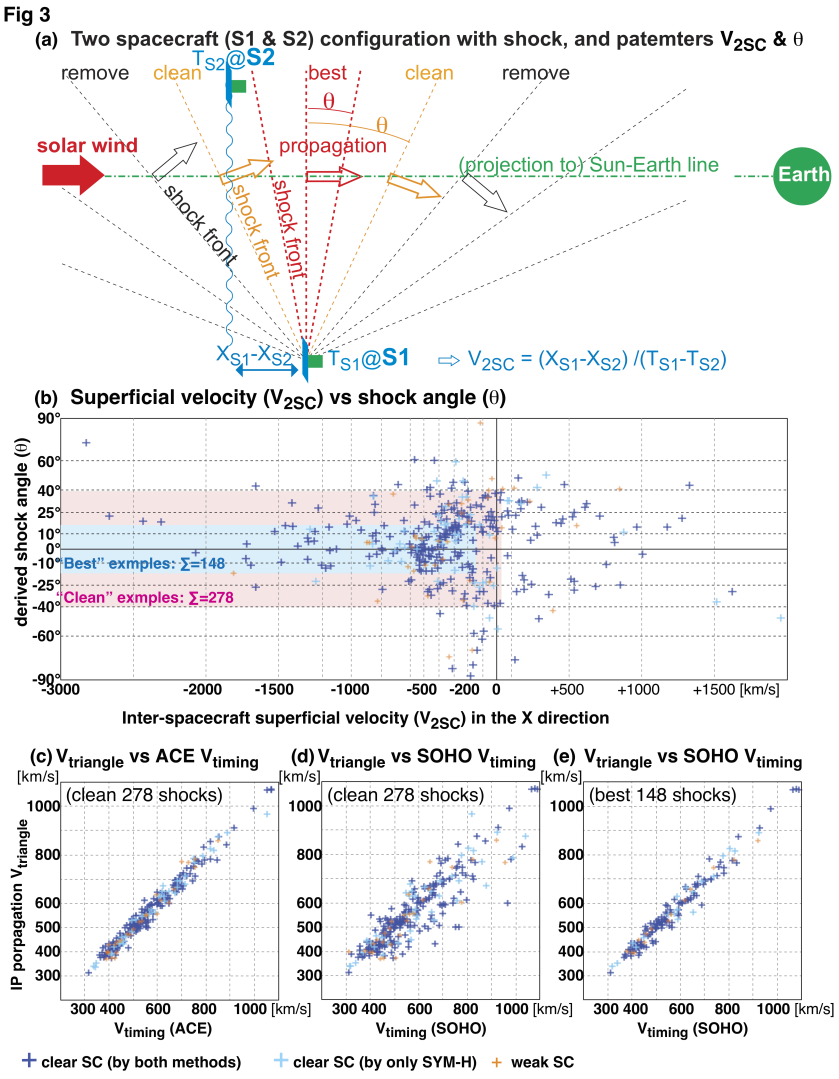

Figure 3. (a) Illustration of general configuration of the IP shocks (dashed lines) propagating (empty arrows) through two spacecraft (S1 and S2) that represent SOHO and ACE. Different colors represent different datasets (best, clean, and consistent) in terms of shock angle (θ). (b) Scatter plot of shock angle (θ) against the simple inter-spacecraft propagation velocity (V_{2SC}) assuming 1D shock pointing anti-sunward. The "consistent" 375 IP shocks are plotted (some shocks are outside the range and not plotted). The red-hatched area ("clean" shocks) is defined by $V_{2SC} < +50$ km/s and $|\theta| < 40°$. The blue-hatched area ("best" shocks) is defined by -3000 km/s $< V_{2SC} < -150$ km/s and $|\theta| < 17°$ (i.e., $|\tan\theta| < 0.3$). (c) Scatter plot of propagation velocity using the IP shock passage timing of two spacecraft ($V_{\rm triangle}$) according to Eq. (1) and that using only one spacecraft ($V_{\rm timing}$) for ACE. All the "clean" 278 IP shocks (red-hatched area) are plotted. (d) The same as (c) but for SOHO. (e) The same as (d) but potted only 148 "best" IP shocks. For all panels, the data are classified into three types in terms of clearness of the SC signature in the same manner as Fig. 2a.

Table 1. Different subsets of IPs

Number of IP shocks	Cleaning level
438 "basic samples"	Clear IP shock & geomagnetic SC are identified by SOHO &SYM-H
375 "consistent" samples out of 438	IP shock profile is consistent between SOHO and ACE
278 "clean" samples out of 375	Downstream s/c detects before upstream s/c & shock angle < 40°
148 "best" samples out of 278	Finite Earthward inter-spacecraft propagation & shock angle < 17° ($\|\tan\theta\| < 0.3$)

through Eq. (2) is clearly a good criterion. Here we assumed the tilt only in the X–Y direction as mentioned in Sect. 2.1 (with only two spacecraft, one must assume tilt direction within one 2D plane in 3D space).

In addition to θ, we have another criterion: the spacecraft locating farther away from the Sun (i.e., smaller $X_{\rm GSE}$) should detect the IP shock after the spacecraft locating closer to the Sun (i.e., larger $X_{\rm GSE}$). To formulate this, we define one more parameter representing the (superficial) inter-spacecraft propagation velocity in the $-X_{\rm GSE}$ direction ($V_{\rm 2SC}$): this is obtained only from the difference of the $X_{\rm GSE}$ locations (S1 and S2 in Fig. 3a) and timing of the IP shock detection ($T_{\rm S1}$ and $T_{\rm S1}$ in Fig. 3a) at SOHO and ACE. If the shock is propagating more or less along the $-X_{\rm GSE}$, the derived speed should be negative ($V_{\rm 2SC} < 0$).

Fig. 3b shows the scatter plot between $V_{\rm 2SC}$ and θ. Using $V_{\rm 2SC}$ and θ, we classified the 375 consistent shock examples in terms of different levels of "cleanness", as summarized in Table 1. In Fig. 3b, there are many cases that are judged "backward" propagation (downstream spacecraft detected the IP shock earlier than the upstream spacecraft), indicating that the IP shock front must be quite tilted toward the Y and/or Z directions. We filtered out these cases in making a clean dataset. Here, we allow a wider range for $V_{\rm 2SC}$ compared to the solar wind speed range even for the best samples, because the inter-spacecraft time difference of the IP shock detection can be as short as 1 min, with possible error of a factor of 2 or more. We also filtered out the IP shocks in which the derived tilt angle (θ) is large.

In Fig. 3b, the red-hatched area selects the IP shocks with $V_{\rm 2SC} < +50$ km/s (removing backward superficial propagation) and $|\theta| < 40°$ (removing obliquely aligned shock). There are total 278 examples of such "clean" shocks. This is already a fairly good dataset as shown in Fig. 3c: the derived propagation velocities using two spacecraft ($V_{\rm triangle}$) and those using only one spacecraft ($V_{\rm timing}$) are well correlated for ACE,

However, the agreement with $V_{\rm timing}$ for SOHO (Fig. 3d) is not as good as for ACE. This is most likely due to the larger distance from the upstream point to the Earth to SOHO (up to 7×10^5 km) than to ACE (up to 3×10^5 km), as mentioned above. To make even a cleaner dataset, we tighten the criterion as -3000 km/s < $V_{\rm 2SC} < -150$ km/s and $|\theta| < 17°$ (i.e., $|\tan\theta| < 0.3$) to form "best" set of the IP shocks (148 examples). The blue-hatched area corresponds to these best IP shocks. For this dataset, the derived propagation velocities using two different methods are well correlated even for SOHO, as shown in Fig. 3e. A list of timings of the IP shock detection and geomagnetic SC for 438 IP shocks, including the classification of difference sub-dataset, is listed in Appendix B (Tables A1-4).

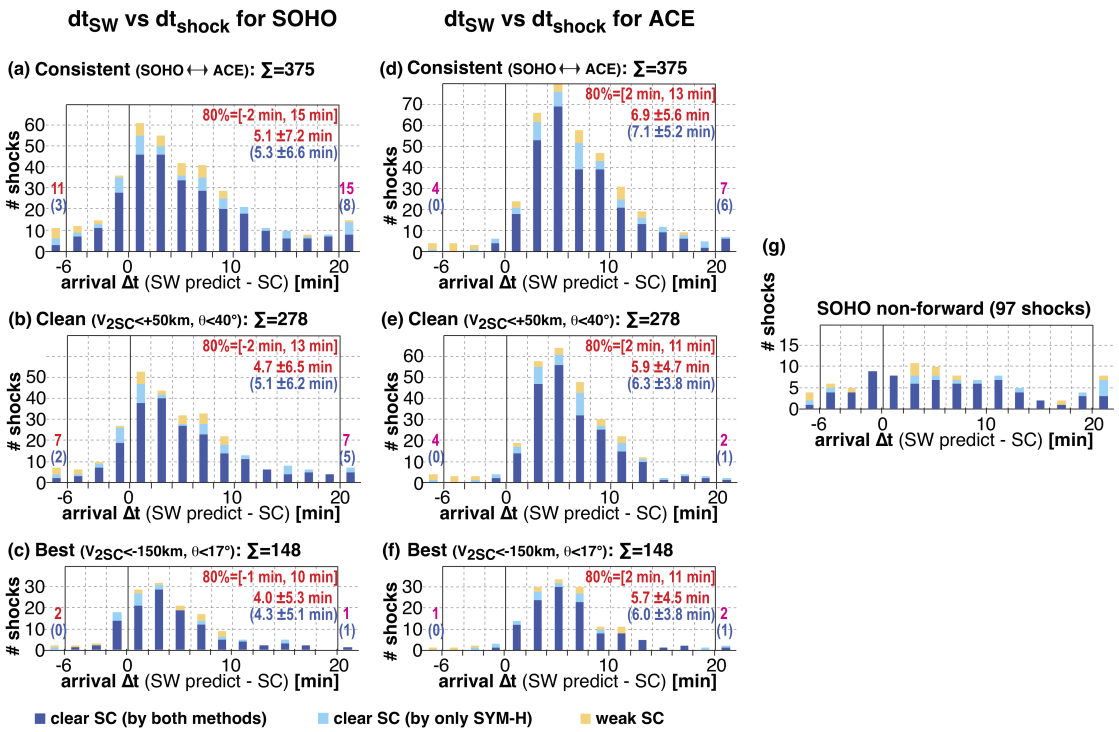

Figure 4. Histogram of time difference Δt between the arrival times of the IP shock at the Earth using the geomagnetic SC signature in SYM-H ($T_{\rm SC}$), and the expected travel time of the solar wind using the fastest solar wind speed within 15 min from an IP shock for (a)-(c) SOHO and (d)-(f) ACE. Top panels (a) and (c) show the distributions of 375 "consistent" IP shocks, middle panels (b) and (e) show the distributions of 278 "clean" IP shocks, and bottom panels (c) and (f) show the distributions of 148 "best" IP shocks, as defined in Fig. 3b and Table 1. (g) The same histogram for removed samples from (a) to (b) for SOHO, i.e., difference between (a) and (b). In each panel, values at the upper right part show the 80% range of the distribution, followed by the average value and the standard deviation. The values inside the parenthesis represent only those with the geomagnetic SC signature detected by two methods. The values at lower left and right edges show the summation of extreme values for both negative (< -6 min) and positive (> +20 min) sides, respectively. Positive Δt means that the actual arrival of the IP shock to the Earth is earlier than the predicted arrival time using the solar wind speed measured by SOHO or ACE. The data are classified into three types in terms of clearness of the SC signature in the same manner as Fig. 2a.

3 Results

Fig. 4 shows the statistics of the time difference Δt for SOHO (left panels) and ACE (middle panels). The format of each panel is the same as Fig. 2b. Figs. 4a and 4d show the distributions of all 375 consistent IP shocks, Figs. 4b and 4e show the distributions of clean subset (278 samples), and Figs. 4c and 4f show the distribution of the best subset (148 samples), as is described in the previous section.

For both SOHO and ACE, Δt values of 375 consistent IP shocks (Figs. 4a and 4d) are distributed wide spread (central 80% range and standard deviations (STD) are -2 to $+15$ min (STD=7.2 min) for SOHO, and $+2$ to $+13$ min (STD=5.6 min) for

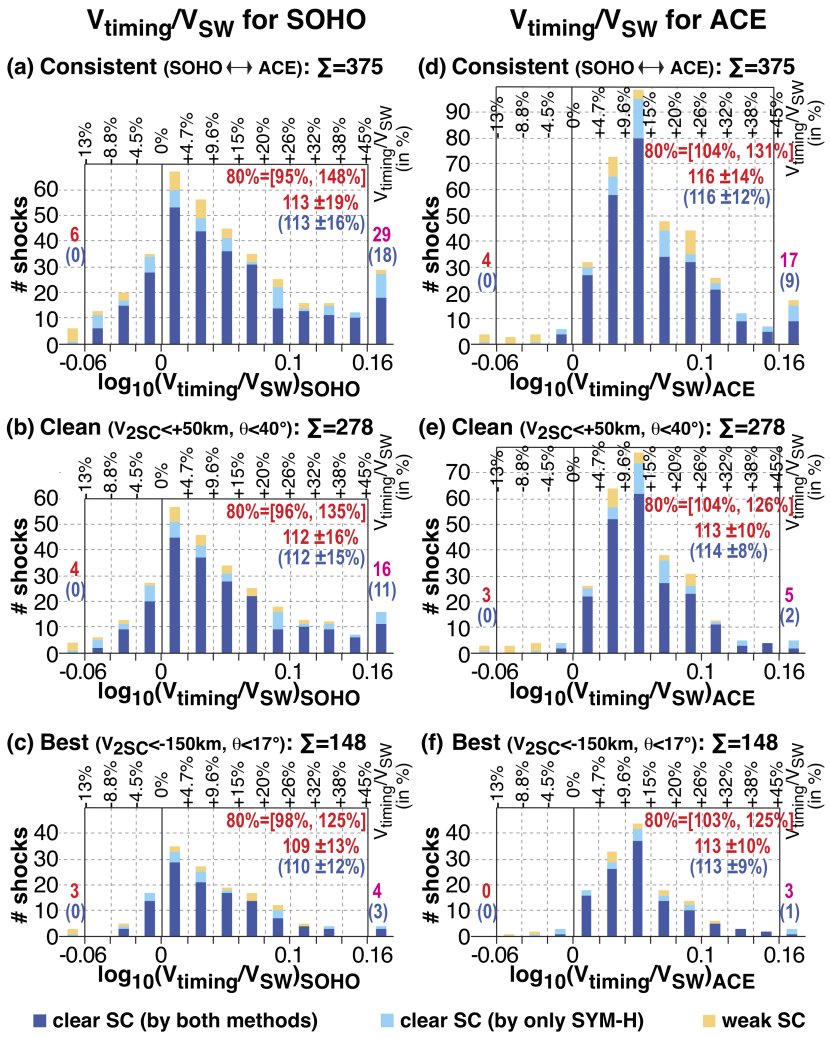

Figure 5. The same as Fig. 4, but for the velocity ratio between the solar wind proton velocity ($V_{\rm SW}$) and the IP shock's propagation velocity ($V_{\rm timing}$). The latter is calculated using the time difference and $X_{\rm GSE}$ distance between the IP shock passage at (a)-(c) SOHO or at (d)-(f) ACE, and the Earth (the geomagnetic SC signature is used for timing at the Earth). To linearize the binning of velocity ratio, we plotted against in a logarithmic scale. For examples, -0.06 and 0.06 correspond to 87% (i.e., 13% slower propagation speed than the solar wind speed) and 115% (i.e., 15% faster), respectively. These differences are written at the top of each panel.

ACE). The distribution is more compact in the best dataset (Figs. 4c and 4f) with central 80% range -1 min to $+10$ min with STD=5.3 min for SOHO, and $+2$ min to $+11$ min with STD=4.5 min for ACE. The numbers of extreme Δt examples (< -6 min or > 20 min) also decreases from 26 to 3 for SOHO and 11 to 2 for ACE for the best 148 examples compared to the consistent 375 examples. In fact, the removed examples (Fig. 4g) show much flatter distribution than clean and best example, consistent with wide error for oblique shocks as explained in the introduction. This fact endorses our filtering method given in

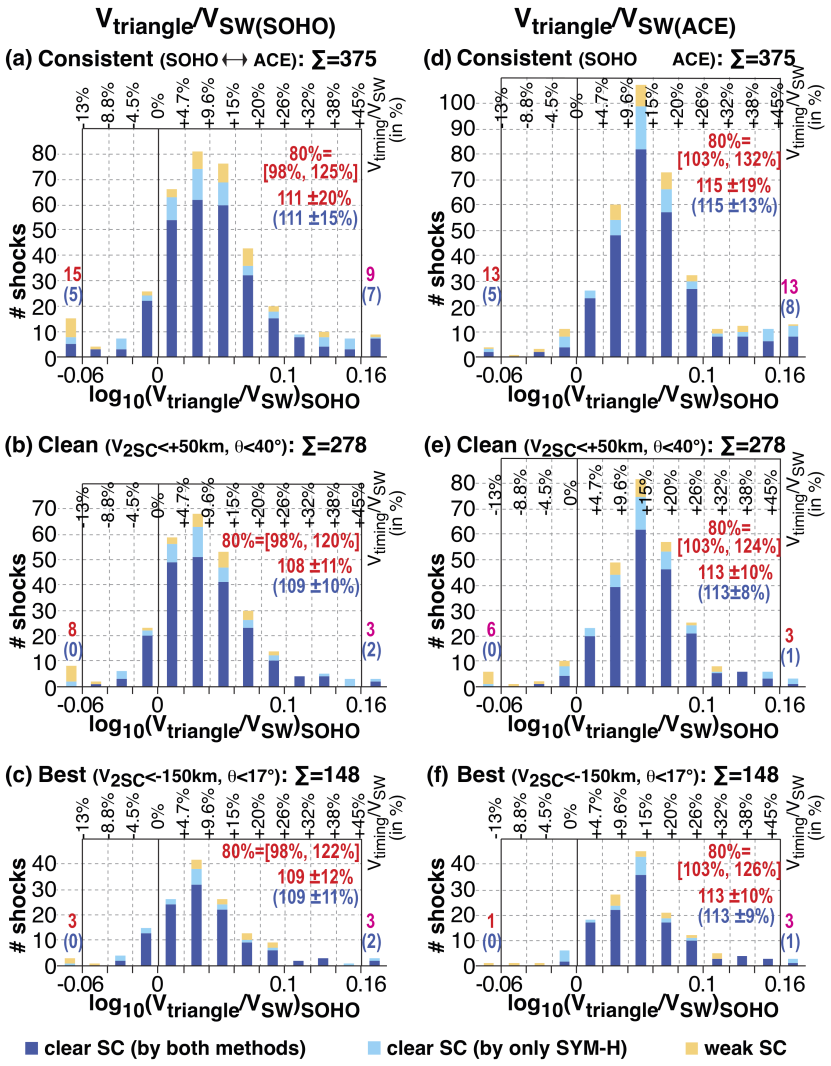

Figure 6. The same as Fig. 5, but instead $V_{\rm timing}$, using $V_{\rm triangle}$ that is estimated according to Eqs. (1) and (2).

Fig. 3b and Table 1. In all panels, the center of Δt is shifted toward the positive side; i.e., the IP shock generally arrives earlier than the predicted arrival time calculated from the measured solar wind speed at L1, as is expected from the shock theory. The earlier arrival of the IP shock to the Earth than the solar wind itself is valid in almost all cases, and negative Δt is most likely a part of spread of the distribution, which is expected as the statistical property of the oblique shock plane, as explained in Introduction.

Fig. 5 shows the velocity ratio $V_{\rm timing}/V_{\rm SW}$ for SOHO (left panels) and ACE (right panels) in the same format as Fig. 4, where $V_{\rm SW}$ is the solar wind proton velocity and $V_{\rm timing}$ is the IP shock's propagation velocity using only one spacecraft. The results for $V_{\rm triangle}$ derived according to Eq. (1) using two spacecraft, instead of $V_{\rm timing}$, are shown in Fig. 6. Since we consider

the ratio, we linearized the binning by taking logarithmic scale, i.e., we plotted the distribution against log10($V_{\rm timing}/V_{\rm SW}$). The resultant distributions are similar to those of Δt in Fig. 4. For the 148 best examples, $V_{\rm timing}$ is -2 to $+25\%$ (central 80%) faster (negative sign means slower) than the solar wind speed for SOHO ($+3$ to $+25\%$ for ACE), with the simple average and standard deviation of $log10(V_{\rm timing}/V_{\rm SW})$ as 0.039 and 0.052 ($+9 \pm 13\%$ difference) for SOHO as shown in Fig. 5c ($+13 \pm 10\%$ difference for ACE, as shown in Fig. 5f).

These averages are unchanged if we use $V_{\rm triangle}$ (which is common for SOHO and ACE) instead of $V_{\rm timing}$ for both SOHO and ACE, as shown in Fig. 6. Even the standard deviation is nearly unchanged by using $V_{\rm triangle}$ (reduced only by 1% for SOHO and unchanged for ACE). Also, the number of extreme cases (i.e., more than 32% faster) is nearly unchanged (for SOHO case, 8 shocks when using $V_{\rm timing}$ and 7 shocks when using $V_{\rm triangle}$). However, the distribution with respect to the average value becomes more symmetric (some asymmetry remains, though) by using $V_{\rm triangle}$ than using $V_{\rm timing}$, particularly for the SOH case, with a reduced 80% range.

4 Possible error sources

In all estimate using timings at L1 and the Earth to derive the propagation speed (Figs. 5 and 6), the shock propagation is faster than the solar wind flow, as is predicted from the shock theory for the forward shock (cf. Appendix A). The differences in the speed is about 9% (-2% to $+22$-25% for central 80%) for SOHO and about 13% ($+3$ % to $+25$-26%.) For such a small differences, we must consider possible sources of the uncertainty in the measurements (solar wind speed and timings) before using this value (about 10% difference) to compare with any models that predicts faster propagation speed than the solar wind speed.

4.1 Velocity value

One question is the accuracy of the velocity values. Although the SOHO proton monitor velocity is well calibrated against those measured by other SOHO instruments and other monitoring spacecraft such as Wind, with a difference less than 1% and a spread less than 3% (e.g., Ipavich, 1998), the calibration is not made during the IP shock passage when the shock speed suddenly increases. In such conditions, a saturation effect is expected, particularly for ACE. Actually the SOHO–ACE difference in Fig. 6 indicates that the measured speed is smaller (difference is larger) by the ACE observation than by the SOHO observation. However, this type of saturation, if any, is less likely alter the result, as described below.

Fig. 7 shows the scatter plots using SOHO data (the same format as Fig. 2a) for the best 148 samples. The left panel shows Δt against the predicted travel time (corresponding to Fig. 4c), the middle panel shows propagation velocity $V_{\rm timing}$ against the solar wind proton velocity $V_{\rm SW}$, and the right panel shows $V_{\rm timing}/V_{\rm SW}$ in logarithmic scale against the measured solar wind speed by SOHO (corresponding to Fig. 5c). If the saturation of the instrument is the reason, we expect more spread for faster solar wind (shorter travel time). However, Fig. 7 shows that the spread in Δt or $V_{\rm timing}/V_{\rm SW}$ does not depend very much on the solar wind speed. Thus, the possible uncertainty in velocity measurement, if any, is not the cause of about 10% faster propagation speed of the shock than $V_{\rm SW}$.

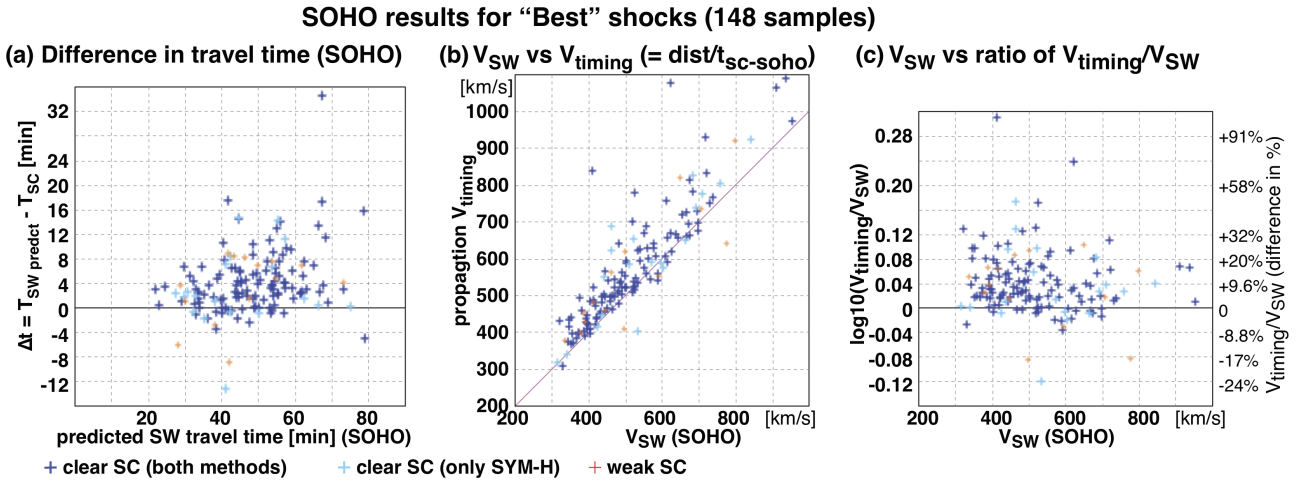

Figure 7. Scatter plot of the best 148 IP shocks in the same format as Fig. 2a for SOHO observation: (a) Δt against the predicted solar wind travel time in the $X_{\rm GSE}$ direction (from SOHO to the Earth); (b) $V_{\rm timing}$ against $V_{\rm SW}$; (c) the ratio velocity log10($V_{\rm timing}/V_{\rm SW}$) against the solar wind velocity.

4.2 Change of speeds from L1 to the Earth

It is possible that an IP shock propagation is decelerated while the solar wind is accelerated, like the high-speed CME near the Sun (Yashiro et al., 2004). If the speed changes, we have to correct the solar wind speed to the average speed between L1 and the Earth, because the shock propagation speed is derived as an average value from start-end timings in this paper. Although the velocity measurements are statistically consistent between the L1 monitoring spacecraft and the Earth orbiting spacecraft (e.g., Ipavich, 1998), the same argument as above applies here (i.e., measurements near the IP shocks can be different from relatively constant solar wind). If such acceleration is substantial, the real offset in $V_{\rm timing}/V_{\rm SW}$ (and Δt) would be smaller than the present result. However, the distance from L1 to the Earth is only 1% of the distance from the Sun to the Earth. We are not aware of any quantitative model that predicts substantial acceleration of the solar wind (or substantial deceleration of the IP shock) within such a short distance. Therefore, this is again less likely cause of about 10% difference between $V_{\rm triasngle}$ and solar wind velocity $V_{\rm SW}$.

4.3 Transit time from the magnetopause to the Earth

The onset timing of the geomagnetic SC was used as the proxy of the timing when the IP shock passing the Earth's terminator. Considering about 10^5 km distance from the magnetopause to the Earth, the travelling time of the IP shock (speed of about 400-900 km/s as shown in Fig. 7c) to the terminator is estimated about 1-3 min. On the other hand, the effect of the enhanced magnetopause current propagates to the Earth (to cause the geomagnetic SC) propagates with about magnetosonic speed (not

the speed of light), resulting in the similar travel time of 1-3min. Therefore, the resultant uncertainty in Δt should be, if any, only 1-2 min.

If we are to improve the accuracy of Δt, we need to monitor the magnetopause location. The Smile satellite (Wang et al., 2025), recently launched in May 2026, can monitor the magnetopause compression using soft X-ray imaging (Sambay et al., 2025). Although the instrument design is 5-min resolution, this can go down to a few minutes for strong IP shocks. Then, we may still have a better accuracy of Δt if we have many IP shocks.

4.4 Tilt of the shock front in the $Z_{\rm GSE}$ direction

Using Eq. (2), we estimated the tilt angle of the shock normal θ in the GSE X-Y direction from the relative timing of IP shock detection between two spacecraft, but with some assumptions such as 2D plane as the shock front and ignoring the gradient and tilt in the $Z_{\rm GSE}$ direction. This is the optimum assumption when we have only two spacecraft to estimate the tilt direction in 3D space, because the tilt direction most likely reflect the offset direction of the source CME on the solar surface, which is distributed all longitudes but only in a limited latitude range near the equator.

However, the shock front may not be ideal 2D plane, and even if so, the tilt angle in the $Z_{\rm GSE}$ directions (θ_Z) can be substantial, as the large discrepancy in the Fig. 1 event indicates. Thus, trusting the derived θ based on Eq. (2) to obtain the propagation velocity $V_{\rm triangle}$ may introduce different types of errors.

To minimize this problem, we used θ only for filtering the best set of IP shocks: we selected the best examples for which the shock normal is expected to point more or less to the $-X_{\rm GSE}$ direction such that this error (which is expected to show symmetric distribution in both positive and negative directions) become relatively small. The success of the filtering is seen in Figs. 3c-3e: for the best 148 IP shocks, all three estimates of the propagation velocity, one by ignoring the tilt in the $Z_{\rm GSE}$ direction ($V_{\rm triangle}$) and the other two by ignoring both in the $Y_{\rm GSE}$ and $Z_{\rm GSE}$ directions ($V_{\rm timing}$), are well correlated to each other, as shown in Figs. 3c and 3e.

To examine if the dataset can be improved by further filtering in terms of possible tilt in the $Z_{\rm GSE}$ direction (assuming no tilt in the $Y_{\rm GSE}$ direction), we sorted the best examples into $|\theta_Z| < 40^\circ$ and $|\theta_Z| > 40^\circ$, and compared the observed propagation speed against the solar wind speed. The distribution of $|\theta_Z| < 40^\circ$ cases and $|\theta_Z| > 40^\circ$ cases are similar to each other, except that this filtering removes all but one case of $V_{\rm triangle} < V_{\rm SW}$ for SOHO (cf. Appendix A for detail). To keep total numbers of samples (and statistical liability), we do not make further filtering by θ_Z for the main distribution.

5 Summary and Discussion

We examined IP shocks that have consistent velocity profiles between SOHO and ACE data during 1998-2022. To remove IP shocks with shock normal largely tilted from the $-X_{\rm GSE}$ direction, we used two parameters as shown in Fig. 3b to obtain 278 clean shocks and 148 best shocks. Statistics of the IP shock during 1998-2022 shows that the geomagnetic SC takes place generally earlier than the predicted solar wind arrival time using the measured solar wind speed at L1 (even using the highest

proton speed within 15 min after the IP shock passage). Thus, as is expected from the shock theory, the IP shocks observed by SOHO and ACE propagate to the Earth faster than the solar wind.

For the 148 "best" IP shocks, the time difference Δt (positive value for earlier geomagnetic SC) spreads over -1 to $+10$ min (central 80% range) for SOHO and $+2$ to $+11$ min for SOHO, with a finite number of IP shocks (15 shocks for SOHO and 22 shocks for ACE out of 148 samples) arrived more than 10 min earlier than the predicted solar wind arrival time as shown in Figs. 4c and 4f. The corresponding propagation speed of the IP shock (derived from the timing and $X_{\rm SGE}$ distance of the spacecraft) for the best 148 shocks (Figs. 5c and 5f) is 9% faster than the solar wind speed for SOHO (13% for ACE), with individual $V_{\rm timing}/V_{\rm SW}$ values ranging from -2% to $+25\%$ ($+3$ to $+25\%$ for ACE). The result is unchanged if the propagation speed ($V_{\rm triangle}$) is estimated using both spacecraft and geomagnetic SC according to Eqs. (1) and (2), except that the distribution becomes more compact (-2% to $+22\%$ for SOHO) as shown in Fig. 6c.

Let us compare the average differences between the IP propagation speed and the solar wind speed (about 10%) with the simple 1D shock model (Eq. (A1) in Appendix A). Here one must note that the model requires density and normal speed of both before and after the shock passage (four measured values) instead of only post-shock speed (one measured value) for $V_{\rm triangle}$, and that the resultant shock propagation speed $V_{\rm 1D}$ is very sensitive to the density ratio between before and after the shock, particularly when the ratio is near unity, as shown in Fig. A1e in Appendix A. Since the density value right after the shock passage can be underestimated due to possible saturation of the instrument, the calculated $V_{\rm 1D}$ can be significantly overestimated particularly the density ratio is close to unity. This saturation is seen in the sparse spread of $V_{\rm 1D}/V_{\rm SW}$ values in Fig. A2 in Appendix A (this is why we show this figure in Appendix rather than in the main text).

Removing these overestimated cases, Fig. A2c indicates that a simple 1D model has the dense cluster of $V_{\rm 1D}/V_{\rm SW}$ around $+10\%$, which is consistent with the observed speed ($V_{\rm triangle}/V_{\rm SW}$), although individual cases are not well correlated. This indicates that the simple 1D model is a good guide in estimating the shock propagation speed near the Earth, encouraging development of measurement method of density right after the shock, as well as detailed analyses in future, e.g., using three or more spacecraft.

In both Figs. 4 and 5, the distribution is slightly asymmetric with respect to the average value (around $+10\%$) with the positive side having a longer tail. This asymmetry is seen as the shift of simple average of Δt in Figs. 4c and 4f (+4 min for SOHO and +6 min for ACE for the best IP shocks) toward larger values than the most frequent Δt (2-4 min for SOHO and 4-6 min for ACE), and the shift of velocity difference ($V_{\rm timing}/V_{\rm SW}$) for SOHO toward faster propagation than the most frequent $V_{\rm timing}/V_{\rm SW}$ (Fig. 5c). Although this asymmetry is reduced for $V_{\rm triangle}$ (using both spacecraft) instead $V_{\rm timing}$ (using only one spacecraft) as shown in Figs. 6, the asymmetry remains, particularly for extreme values (e.g., out of 148 best shocks, 9 shocks are $> +26\%$ (all are with a clear SC signature of > 10 nT in SYM-H) faster than the SOHO solar wind speed, whereas 4 are slower by 9%. The preference toward positive extreme is enhanced if either we remove weak shocks (only one example of negative extreme) or we remove $|\theta_Z| > 40^\circ$ cases in possible tilt in the $Z_{\rm GSE}$ direction (no example of negative extreme as shown in Fig. A2c). Thus, the $V_{\rm triangle}/V_{\rm SW}$ distribution is most likely asymmetric toward higher values (toward faster propagation) with respect to the central part of the distribution (which is already higher than unity), although statistics is not

sufficient. So far, we have no solid explanation for this long tail, and it is worth examining these extreme cases in the light of shock models in future, e.g., using more spacecraft such as the DSCOVER and Wind (this is outside the scope of this paper).

If only one spacecraft is used, the spread of Δt is as wide as Fig. 2b (and Fig. 4a), with a substantial fraction arriving > 10 min earlier than the predicted time. This means that one must be ready for possible space weather hazard starting earlier than the predicted arrival time based on the real-time L1 monitor, although one can expect, in average, the shock propagation about 1.1 times faster than the observed solar wind speed. This fact also warns the usage of 1-min resolution solar wind OMNI data at the magnetopause (https://omniweb.gsfc.nasa.gov/), in which the same propagation speed as the measured solar wind speed is used when projecting the L1 observation to the magnetopause nose (Omniweb, 2026).

6 Conclusions

As is expected from the shock theory, the IP shocks observed by SOHO and ACE propagate to the Earth faster than the solar wind. We used two spacecraft instead of one to select nearly radially propagating P shocks (shock normal is not tilted very much from the $-X_{\rm GSE}$ direction) as shown in Fig. 3. For the best 148 shock that are selected in this manner, the difference compared with solar wind velocity measure by SOHO, which is slightly higher than that measured by ACE, is about 9% with standard deviation of 12%.

The 9% higher speed with wide spread range in the speed ratio indicates that the simple 1D shock model gives reasonable estimates after we consider the uncertainty in observation, whereas the individual example (such as the case shown in Fig. 1) can be quite different between the estimation by the simple shock model and the actual observation. The average ratio of 1.1 can be applied for real-time prediction of the arrival time of CME-driven forward shock after detection of L1 monitoring spacecraft such as DSCVOR.

Another unexpected feature is asymmetric distribution of the propagation speed compared to the solar wind speed. Although statistics is not sufficient, the distribution of the ratio $V_{\rm timing}/V_{\rm SW}$ is extended to higher values with respect to the center of the distribution (which is already ~ 1.1 instead of unity). We have no answer to it so far.

Data availability. SOHO data is taken from SOHO site (https://l1.umd.edu/) and NASA NASADCC site (https://cdaweb.gsfc.nasa.gov/). ACE data is taken from both ACE site (https://izw1.caltech.edu/ACE/ASC/level2/index.html) and NASA NASADCC site (https://cdaweb.gsfc.nasa.gov/). Geomagnetic indices are taken WDC-C2 for geomagnetism, Kyoto University (https://wdc.kugi.kyoto-u.ac.jp/wdc/Sec3.html). Another list of geomagnetic sudden commencement is found at Ebre Observatory data portal (https://www.obsebre.es/en/variations/rapid).

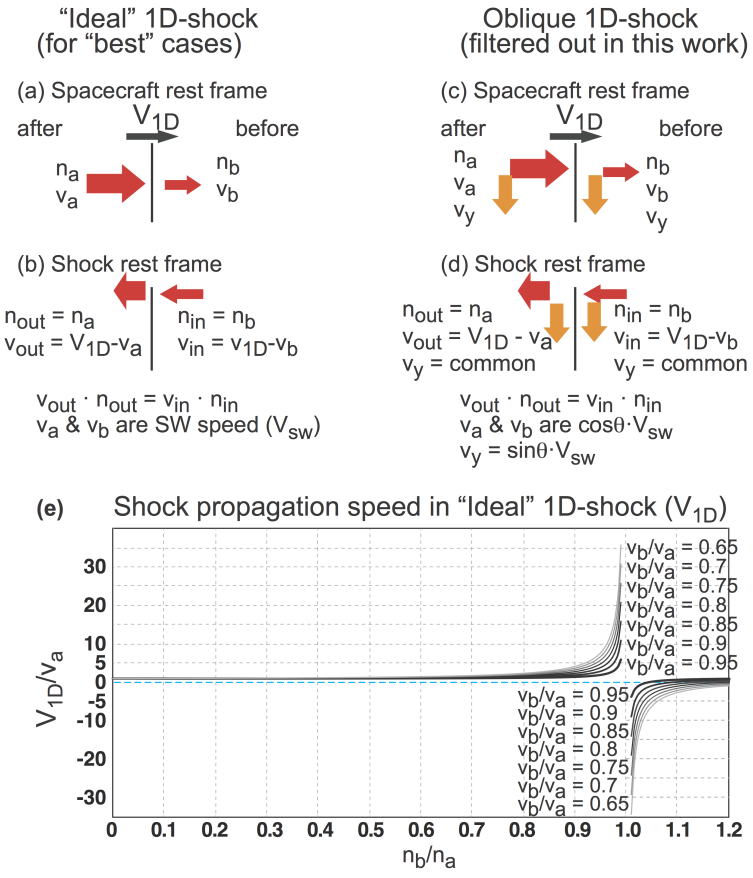

Figure A1. (a) and (b) Illustration of mass flux ($n \cdot v$, where n is density and v is 1D speed) conservation across the simplest 1D shock in (a) spacecraft rest frame and (b) shock rest frame. (c) and (d) A more general 1D shock case with finite flow velocity along the shock surface. (e) Theoretical values V_{1D}/v_a (ratio between the shock propagation speed V_{1D} and the flow speed after the shock v_a) versus n_b/n_a (inverse of the shock compression ratio) for different velocity changes. Suffix "a", "b", and "sh" in the upper panel denote after the shock passage, before the shock passage, and shock front, respectively. Suffix "in" and "out" in the lower panel denote the inflow to the shock and outflow from the shock, respectively.

Appendix A: 1D-shock mass flux conservation relation

Fig. A1 illustrates the mass flux conservation relation for a textbook-type 1D shock. Through conservation relation in the shock frame, the density n and velocity normal to the shock v in the spacecraft frame has a relation of

$$n_a \cdot (V_{1D} - v_a) = n_b \cdot (V_{1D} - v_b)$$

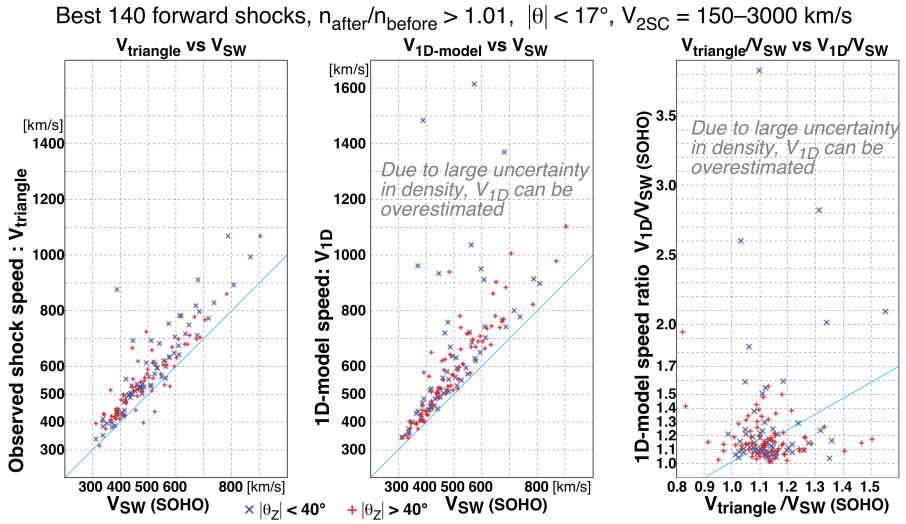

Figure A2. Scatter plot of 140 IP forward shocks (selected from the 148 best shocks) between different estimates of the shock propagation speed and $V_{\rm SW}$ by SOHO observation: (a) $V_{\rm triangle}$ that is estimated according to Eqs. (1) and (2); (b) $V_{\rm 1D}$ that is estimated according to Eq. (A1); (c) $V_{\rm triangle}/V_{\rm SW}$ versus $V_{\rm 1D}/V_{\rm SW}$. Different symbols mean the different tilt angles (θ_Z) toward the GSE Z direction (blue cross: $|\theta_Z| < 40°$; red plus: $|\theta_Z| > 40°$) assuming uniform in the GSE Y direction (which is less likely than the opposite assumption). The solar wind values used in these specific plots are 10 min average values over 3-13 min before the shock and 3-13 min after the shock.

or

$$(V_{\rm 1D}/v_a) = \frac{1-\epsilon\cdot(v_b/v_a)}{(1-\epsilon)} \qquad \text{(A1)}$$
$$> 1 \ \ (\text{for forward shock})$$

where $\epsilon = (n_b/n_a) < 1$ is inverse of the shock compression ratio, and suffix "a", "b", and "sh" denote after the shock passage, before after the shock passage, and shock front, respectively.

This relation is unchanged when the flow component along the shock front (v_y) is added (cf. Figs. A1c and A1d), as long as v_y is the same between the upstream and downstream (i.e., no vorticity is carried by the shock). We just need to use $V_{\rm SW}\cdot\cos\theta$ instead of $V_{\rm SW}$ as the values of v_a and v_b in this case, where θ is the tilt angle of the shock normal compared to the solar wind direction. Since we consider small θ cases, we ignore the difference between $V_{\rm SW}\cdot\cos\theta$ and of $V_{\rm SW}$ in this paper.

Although Eq. (A1) provides $V_{\rm 1D}/v_a$, one cannot simply trust the derived values in the actual shock observations because of the high uncertainty in the solar wind measurement (particularly density) right after the shock: n_a (and possibly v_a) can be significantly underestimated due to saturation of the ion instrument, as explained in Sect. 2. This makes overestimation of n_b/n_a values for some shocks, making them much closer values to unity than it actually is. As shown in Figs. A1e, the $V_{\rm 1D}/v_a$ value is very sensitive to n_a value near $n_b/n_a = 1$, making small underestimation of n_a resulting in large overestimation of $V_{\rm 1D}$ (and $V_{\rm 1D}/V_{\rm SW}$). This is why we did not show the distribution plots of $V_{\rm 1D}/V_{\rm SW}$.

We instead show scatter plot in Fig. A2, comparing V_{1D} (theoretical 1D shock speed according to Eq. (A1) using density and velocity values of SOHO both before and after the shock), $V_{triangle}$ (observed propagation speed using timings of shock passage at SOHO, ACE, and the Earth according to Eqs. (1) and (2)), and V_{SW} measured by SOHO. Since the density is more variable than the velocity, we took average values over 10 min periods for the solar wind values in Fig. A2: 3-13 min before the shock and 3-13 min after the shock. Nevertheless, there are several cases when the density values superficially decreased after the shock even it is forward shock according to the ACE data. We removed such obvious cases and also reverse shock in Fig. A2.

After normalized by V_{SW} (Fig. A2c), values of $V_{triangle}/V_{SW}$ and V_{1D}/V_{SW} fall into the same range (majority around $+10\%$) although they are not well correlated if we look into in detail. Considering possible overestimation for some cases, and other uncertainty (cf. Sect. 4), the simple 1D model gives good estimate of the actual propagation speed.

Finally, the effect of tilt angle in the Z_{GSE} (θ_Z) is examined by subdividing the dataset into between $|\theta_Z| < 40°$ and $|\theta_Z| > 40°$, by assuming uniform in the Y_{GSE} direction. If removing obviously overestimated case, no outstanding difference is seen between $|\theta_Z| < 40°$ cases and $|\theta_Z| > 40°$ cases in terms of V_{1D}/V_{SW} (Figs. A2b and A2c)). On the other hand, removing $|\theta_Z| < 40°$ cases makes the distribution of $V_{triangle}/V_{SW}$ slightly more compact, as is expected from analogy to filtering by tilt angle toward Y_{GSE} (θ). As the result, the distribution of $V_{triangle}/V_{SW}$ ratio for the most filtered IP shock (blue cross in Fig. A2c) is slightly asymmetric toward higher ratio with respect to the center of the distribution (around $+10\%$).

Appendix B: Timing list of IP shocks

Table A1 lists the timings of the best 148 IP shocks (see Table 1) that are used in making Figs.3c, 3f, 4c, and 4f. The second and third columns show the UT of IP shock detection by SOHO and by ACE, respectively. The fourth column shows the onset UT of sudden increase of SYM-H. The last column indicates the clearness of the SC (see caption of Fig. 2).

In the same format, Table A2 lists the timings of the remaining 130 IP shocks other than the best 148 shocks (after removing the samples listed in Table A1) out of 278 "clean" IP shock in Table 1. This subset is used in making Figs 6b.

Similarly, Table A3 lists the timings of the remaining 97 IP shocks (after removing the samples listed in Tables A1 and A2) out of 375 "consistent" IP shock on Table 1. This subset is used in making Figs 6a.

Finally, Table A4 lists the timings of the 63 IP shocks with only SOHO data (after removing the samples listed in Tables A1–A3) out of 438 "basic samples" IP shock in Table 1.

Author contributions. MY and YY initiated the work. YY made overview plots related to SOHO and ACE in several format for all the events, and prepared tables that contain the velocity, timing, and the expected transit time. MY made the sub-dataset of the geomagnetic SYM-H indices (SYMASY) to identify the onset timing of geomagnetic SC timing, and examined all these plots to revise and complete the table made by YY. TK mainly contributed to SYM-H part, and JM made independent SC list from different dataset. MY made first draft of the text and figures, while all others contributed the text and discussion.

Competing interests. The authors declare that they have no competing interests.

Acknowledgements. SOHO is a project of international cooperation between ESA and NASA. ACE is a NASA project that is aimed as the solar wind monitor during the International Solar Terrestrial Program. Data from both spacecraft are open access. The authors gratefully thank the instrument teams that maintained the quality of the solar wind data at L1 for nearly 30 years that are used in this study: SOHO PM team (PI: F.M. Ipavich), ACE SWEPAN team (PI: D.J McComas), and ACE MG team (PI: N. Ness). The NASA OMINI data at Omniweb site (https://cdaweb.gsfc.nasa.gov/) is maintained by Space Physics Data Facility, NASA Goddard Space Flight Center.

Geomagnetic indices SYMASY and AE are calculated by World Data Center (WDC) for Geomagnetism, Kyoto using geomagnetic field data at SYMASY stations (San Juan, Fredericksburg, Boulder, Tucson, Papeete, Honolulu, Memambetsu, Urumqi, Alma Ata, Alibag, Martin de Vivies, Hermanus, Chambon-la-Foret) and AE stations (Abisko, Amderma, Dixon Island, Cape Chelyuskin, Tixie Bay, Pebek, Cape Wellen, Barrow, College, Yellowknife, Fort Churchill, Sanikiluaq, Great Whale River, Poste-de-la-Baleine, Narsarsuaq, Leirvogur). The geomagnetic SC list at Ebre Observatory (https://www.obsebre.es/en/variations/rapid) is derived from geomagnetic field data at many stations listed there. We thank all these contributing observatories.

Special thank goes to T. Araki (deceased August 2025) who initiate another work for which the produced plots lead this work. Without him, we never started this work. MY is partly supported by Swedish National Space Agency (dnr 2024-00124).

References

Araki, T.: Global structure of geomagnetic sudden commencements, Planet. Space Sc., 25, 373?384, https://doi.org/10.1016/0032-0633(77)90053-8, 1977.

Araki, T.: A Physical Model of the Geomagnetic Sudden Commencement, 183-200, American Geophysical Union (AGU), ISBN 9781118663943, https://doi.org/10.1029/GM081p0183, 1994.

Collier, M.R., Slavin, J.A.,, Lepping, R.P., Szabo, A., and Ogilvie, K.: Timing accuracy for the simple planar propagation of magnetic field structures in the solar wind, Geophys. Res. Lett., 25, 2509-2512, https://doi.org/10.1029/98GL00735, 1998.

Gonzalez-Esparza, A. and Aguilar-Rodriguez, E.: Speed evolution of fast CME/shocks with SOHO/LASCO, WIND/WAVES, IPS and in-situ WIND data: analysis of kilometric type-II emissions, Ann. Geophys., 27, 3957–3966, https://doi.org/10.5194/angeo-27-3957-2009, 2009.

Gopalswamy, N., Yashiro, S., Michalek, G., Stenborg, G., Vourlidas, A., Freeland, S., and R. Howard, R., The SOHO/LASCO CME Catalog, Earth, Moon, Planet., 104, 295-313 https://doi.org/10.1007/s11038-008-9282-7, 2009.

Ipavich, F.M., Galvin, A.B., Lasley, S.E., Paquette, J.A., Hefti, S., Reiche, K.U., et al.: Solar wind measurements with SOHO: The CELIAS/MTOF proton monitor J. Geophys. Res., 103, 17205-17213 https://doi.org/10.1029/97JA02770, 1998.

King, J., and Papitashvili, N.: Explanation of one min and 5-min solar wind data sets at the Earth's bow shock nose of OMNIWeb, https://omniweb.gsfc.nasa.gov/html/omni_min_data.html#3, (last access, 12 February 2026), 2025.

Manoharan, P.K., Tokumaru, M., Pick, M., Subramanian, P., Ipavich, F.M., Schenk, K., Kaiser, M.L., Lepping, R.P., and Vourlidas. A.: Coronal mass ejection of 2000 July 14 flare event: Imaging from near-Sun to Earth environment, Astrophys. J., 559, 1180-1189, https://doi.org/10.1086/322332, 2001.

McComas, D.J., Bame, S.J., Barker, P., Feldman, W.C., Phillips, J.L., Riley, P., and J.W. Griffee J.W.: Solar Wind Electron Proton Alpha Monitor (SWEPAM) for the Advanced Composition Explorer, Space Sci. Rev. 86, 563–612, https://doi.org/10.1023/A:1005040232597, 1998.

Milan, S.E., Carter, J.A., Bower, G.E., Fleetham, A.L., and Anderson, B.J.: Influence of off-Sun-Earth line distance on the accuracy of L1 solar wind monitoring, J. Geophys. Res., 127, e2021JA030212, https://doi.org/10.1029/2021JA030212, 2022

Nanjo, S., Yamauchi, M., Johnsen, M.G., Yokoyama, Y., Brändström, U., Ogawa, Y., Willer, A.N., and Hosokawa, K.: Leaping and vortex motion of the shock aurora toward the late evening sector observed on 26 February 2023, Ann. Geophys., 43, 303-317, https://doi.org/10.5194/angeo-43-303-2025, 2025.

NASA Goddard Space Flight Center: Omniweb Plus https://omniweb.gsfc.nasa.gov/, (last access, 16 June 2026), 2026.

Ogilvie, K.W., Chornay, D.J., Fritzenreiter, R.J., Hunsaker, F., Keller, J., et al.: SWE, a comprehensive plasma instrument for the WIND spacecraft, Space Sci. Rev., 71, 55-77, https://doi.org/10.1007/BF00751326, 1995.

Paularena, K.I., Richardson, J.D., Zastenker, G.N., Dalin, P.A.: Solar wind correlations: Using a solar wind monitor successfully, In: Sibeck, D.G., Kudela, K. (eds) Interball in the ISTP Program. NATO Science Series, vol 537. Springer, Dordrecht. https://doi.org/10.1007/978-94-011-4487-2_12, 1999.

Paularena, K.I., Zastenker, G.N., Lazarus, A.J. and Dalin, P.A.: Solar wind plasma correlations between IMP 8, INTERBALL-1 and WIND, J. Geophys. Res., 103, 14601-14617, https://doi.org/10.1029/98JA00660, 1998.

Richardson J.D., and Paularena, K.I.: The orientation of plasma structure in the solar wind, Geophys. Res. Lett., 25, 2097-2100, https://doi.org/10.1029/98GL01520, 1998.

Sembay, S., Cheney, A., Hampson, R., et al., The soft X-ray imager (SXI) on the SMILE Mission, Space Sci. Rev. 221, 113, https://doi.org/10.1007/s11214-025-01241-y, 2025.

Tokumaru, M., Kojima, M., Fujiki, K., and Yamashita, M.: Tracking heliospheric disturbances by interplanetary scintillation, Nonlin. Processes Geophys., 13, 329–338, https://doi.org/10.5194/npg-13-329-2006, 2006.

Wang, C., Branduardi-Raymont, G., Escoubet, C.P., and Forsyth, C.: Solar wind magnetosphere ionosphere link explorer (SMILE): Science and mission overview, Space Sci. Rev. 221, 9, https://doi.org/10.1007/s11214-024-01126-6, 2025.

Yashiro, S., Gopalswamy, N., Michalek, G., St. Cyr, O.C., Plunkett, S.P., Rich, N.B., and Howard, R. A.: A catalog of white light coronal mass ejections observed by the SOHO spacecraft, J. Geophys. Res., 109, A07105, https://doi.org/10.1029/2003JA010282, 2004.

Table A1: Timing of IP detection and geomagnetic SC for best 148 samples

Date	SOHO	ACE	SYM-H	SC[*1]
19980407	16:58	16:51	17:51	both
19980501	21:14	21:22	21:57	both
19981107	07:34	07:37	08:16	both
19990310	00:45	00:40	01:31	both
19990517	23:53	24:03	24:57	both
19990626	19:26	19:25	20:17	both
19990706	14:22	14:17	15:10	both
19990804	01:30	01:16	02:20	both
19990815	09:51	09:38	10:44	both
19991021	01:33	01:38	02:26	both
19991028	11:16	11:27	12:16	both
20000111	13:51	13:40	14:27	both
20000211	02:21	02:13	02:59	both
20000220	20:56	20:46	21:40	both
20000406	16:01	16:04	16:40	both
20000604	14:17	14:23	15:02	both
20000623	12:33	12:27	13:03	both
20000713	09:10	09:01	09:43	both
20000726	18:08	17:55	18:57	both
20000728	05:53	05:42	06:34	both
20000811	18:18	18:11	18:46	both
20000906	16:18	16:13	17:01	both
20001002	23:58	24:08	24:54	both
20001005	02:35	02:40	03:26	both
20001012	21:35	21:44	22:28	both
20001028	09:00	09:08	09:55	both
20001031	16:22	16:30	17:15	both
20010110	15:28	15:19	16:21	both
20010117	15:45	15:31	16:32	both
20010123	10:15	10:06	10:49	both
20010404	14:20	14:22	14:54	both
20010527	14:17	14:18	14:59	both
20010803	06:37	06:25	07:16	both
20010817	10:26	10:16	11:03	both
20010929	09:03	09:05	09:39	both
20010930	18:41	18:46	19:25	both
20011011	16:12	16:20	17:01	both
20011115	13:45	13:53	15:09	both
20011119	17:34	17:35	18:15	both
20011229	04:56	04:47	05:38	both
20011230	19:39	19:32	20:10	both
20020131	20:44	20:38	21:26	both
20020318	12:32	12:36	13:21	both
20020320[*3]	13:04	13:06	13:28	both
20020323	10:46	10:53	11:36	both
20020329	21:27	21:40	22:37	both
20020417	10:13	10:21	11:07	both
20020423	04:07	04:15	04:49	both
20020511	09:16	09:25	10:14	both
20020523	10:17	10:14	10:50	both
20020725	13:03	12:59	13:37	both
20020729	12:43	12:40	13:22	both
20020801	22:30	22:20	23:11	both
20020818	18:15	18:10	18:46	both
20020930	07:13	07:21	08:16	both
20030408	00:04	00:15	01:12	both
20031024	14:47	14:49	15:25	both
20031120	07:29	07:27	08:03	both
20040122	01:10	01:04	01:36	both
20040403	08:49	08:56	09:48	both
20040409	01:47	01:49	02:33	both
20040412	17:34	17:36	18:17	both
20040726	22:28	22:26	22:49	both
20040730	20:41	20:31	21:14	both
20040913	19:29	19:34	20:02	both
20041107	17:59	17:53	18:27	both
20041205	07:04	06:55	07:47	both
20050121	16:49	16:48	17:11	both
20050528	03:47	03:31	04:37	both
20050529[*3]	09:15	09:03	09:53	both
20050710	02:56	02:47	03:38	both
20050824	05:33	05:38	06:13	both
20050915	08:25	08:29	09:05	both
20060101	13:35	13:30	14:05	both
20060428	00:20	00:11	01:18	both
20061214	13:56	13:52	14:15	both
20080528	01:32	01:28	02:25	both
20090528	04:21	04:16	05:20	both
20091004[*3]	03:15	03:07	04:14	both
20100405	07:59	07:54	08:27	both
20100803	16:51	16:55	17:41	both
20110218	00:41	00:41	01:31	both
20110329	15:13	15:01	16:03	both
20110711	08:05	08:10	08:50	both
20110909	11:49	11:42	12:43	both
20110917	03:05	02:55	03:44	both
20111024	17:50	17:48	18:31	both
20120312	08:45	08:42	09:15	both
20120423	02:29	02:27	03:21	both
20120616	08:52	08:57	09:56	both
20121031	14:46	14:39	15:40	both
20130216	11:12	11:10	12:10	both
20130315	04:46	04:40	05:27	both
20130820	21:43	21:33	22:29	both
20131002	01:24	01:18	01:56	both
20140107	14:24	14:25	15:14	both
20140503	16:51	16:49	17:48	both
20141223	10:30	10:33	11:16	both
20150815	07:49	07:44	08:30	both
20150920	05:32	05:27	06:05	both
20151106	17:32	17:34	18:19	both
20151219	15:27	15:28	16:17	both
20160719	23:09	23:03	23:51	both
20161012	21:25	21:19	22:13	both
20170716	05:18	05:17	06:00	both
20170831	04:49	04:44	05:39	both
20170906	23:13	23:08	23:45	both

20170907	22:38	22:35	23:01	both
20180108	05:59	05:53	06:47	both
20190708	18:38	18:30	19:23	both
20190727	08:12	08:07	09:09	both
20210512	05:45	05:49	06:39	both
20210827	00:28	00:24	01:16	both
20211227	08:51	08:41	09:37	both
20220201	21:42	21:36	22:22	both
19990815	18:47	18:35	19:38	symH
20000711	08:22	08:17	09:16	symH
20010113	01:50	01:43	02:20	symH
20010327	01:03	01:09	01:44	symH
20010818	05:37	05:24	06:14	symH
20020110	15:52	15:44	16:20	symH
20021002	22:08	22:14	22:55	symH
20030620	08:04	07:56	08:37	symH
20041109	18:24	18:20	18:49	symH
20050217	22:00	22:04	22:46	symH
20060818*3	15:41	15:49	16:42	symH
20090114	00:05	00:13	01:20	symH
20110929	00:27	00:20	01:04	symH
20111030	08:56	08:54	10:02	symH
20120904*3	22:12	22:03	22:46	symH
20130525	09:06	09:09	09:49	symH
20130623	03:53	03:56	04:27	symH
20151104	03:23	03:24	03:54	symH
20220723	02:30	02:26	02:58	symH
19980218*3	08:01	07:53	08:44	weak
19981108	04:19	04:21	04:52	weak
19990228	20:46	20:33	21:32	weak
19990823	11:38	11:29	12:24	weak
20000726	03:02	02:53	03:52	weak
20000728	09:19	09:09	09:57	weak
20001028	05:31	05:41	06:40	weak
20021219	13:31	13:17	14:22	weak
20030529	18:36	18:30	19:01	weak
20030717*2	00:13	00:08	00:42	weak
20030727*2	04:42	04:38	05:16	weak
20041205	04:16	04:06	05:11	weak
20140219	03:14	03:09	03:49	weak
20170716	16:58	16:53	17:39	weak

1: Identification of geomagnetic SC by both methods (=2), by only SYM-H (=1), and weak/unclear SC (=?)
*2: Reverse shock
*3: Density measurement is skeptical.

Table A2 Timing of IP detection and geomagnetic SC for better 130 samples

Date	**SOHO**	**ACE**	**SYM-H**	**SC*1**
19980423	17:13	17:28	18:25	both
19980515	13:41	13:57	14:52	both
19980529	14:58	15:03	15:38	both
19990505	14:45	14:59	15:43	both
19990626	02:35	02:18	03:25	both
19991105*3	19:07	19:14	20:10	both
19991212	15:14	15:14	15:52	both
20000127	14:13	13:56	14:53	both
20000211	23:23	23:18	23:53	both
20000214	07:07	06:56	07:33	both
20000719	15:00	14:47	15:26	both
20001104	01:29	01:34	02:21	both
20001106	09:06	09:15	09:49	both
20001128	04:47	04:57	05:31	both
20010303	10:52	10:40	11:22	both
20010319	10:12	10:22	11:14	both
20010322	12:32	12:42	13:42	both
20010327	17:02	17:15	17:47	both
20010331	00:14	00:23	00:52	both
20010408	10:23	10:32	11:02	both
20010417	23:56	24:05	24:47	both
20010421	14:57	15:06	16:01	both
20010428	04:28	04:31	05:00	both
20010812	10:49	10:49	11:35	both
20010914	01:07	01:18	02:05	both
20011021	16:05	16:12	16:47	both
20011025	07:57	08:02	08:50	both
20011028	02:33	02:43	03:19	both
20011031	12:49	12:53	13:49	both
20020419	07:58	08:02	08:35	both
20020510	10:28	10:29	11:24	both
20020518	19:29	19:19	20:08	both
20020520	02:56	02:57	03:41	both
20020719	09:36	09:32	10:09	both
20020801*3	04:44	04:24	05:11	both
20021126	21:21	21:10	21:51	both
20030529	11:53	11:52	12:25	both
20030618	04:44	04:29	05:13	both
20031104	05:53	05:58	06:26	both
20031115	05:27	05:18	05:50	both
20040410	19:26	19:27	20:10	both
20041107	02:22	01:53	02:57	both
20041107	10:22	09:58	10:53	both
20050902	13:32	13:40	14:20	both
20050909	13:10	13:16	14:01	both
20060709*3	21:04	20:46	21:37	both
20070920	09:26	09:05	10:13	both
20071025	10:56	10:38	11:35	both
20090903	14:54	14:46	15:53	both
20100402	06:45	06:35	07:16	both
20100411	12:18	12:13	13:04	both
20110214	15:02	14:56	15:57	both

20110418	06:06	05:56	06:52	both
20110604	19:45	19:58	20:45	both
20110926	12:02	11:52	12:35	both
20111005	06:55	06:46	07:37	both
20111128	21:27	21:15	21:51	both
20120226	21:07	20:56	21:40	both
20120307	03:47	03:35	04:20	both
20120315	12:42	12:35	13:08	both
20120521	18:52	18:44	19:38	both
20120616	19:24	19:30	20:20	both
20120616	20:30	20:31	21:16	both
20120721	15:25	15:34	16:13	both
20120903	11:33	11:22	12:14	both
20120930	22:21	22:13	23:07	both
20121123	21:22	21:11	21:53	both
20130119	16:34	16:46	17:34	both
20130125	16:04	16:00	17:00	both
20130413	22:24	22:13	22:54	both
20130519	22:13	22:20	23:09	both
20130627	13:45	13:52	14:39	both
20131008	19:51	19:40	20:21	both
20140207	16:28	16:17	17:06	both
20140220	02:58	02:51	03:20	both
20140227	16:17	16:07	16:51	both
20140623	22:01	22:02	23:08	both
20140714	13:28	13:30	14:32	both
20140819	06:14	05:58	06:59	both
20141110	01:31	01:36	02:21	both
20141221	18:22	18:23	19:12	both
20150317	04:10	04:03	04:45	both
20150506	00:50	00:53	01:43	both
20151231	00:10	00:02	00:50	both
20161109*3	05:28	05:34	06:44	both
20170708	23:27	23:13	24:11	both
20170914	10:20	10:19	11:16	both
20180419	22:59	23:10	24:22	both
20190510	16:50	16:53	17:55	both
20190526	21:01	21:09	22:15	both
20210526	11:53	11:45	12:45	both
20211127	22:06	21:59	22:52	both
20230315	03:42	03:48	04:28	both
19990221	21:52	21:46	22:41	symH
20000713	09:32	09:19	09:54	symH
20000814	21:48	21:36	22:19	symH
20000915	04:14	03:59	04:49	symH
20010104	13:08	13:07	14:02	symH
20010407	16:44	16:58	17:33	symH
20011001	21:15	21:29	22:02	symH
20020322	03:23	03:23	04:07	symH
20021224	13:18	13:14	13:55	symH
20030509	04:49	04:56	05:20	symH
20030530	16:02	15:53	16:24	symH
20040801	02:02	01:49	02:28	symH
20050801	06:09	06:05	06:37	symH
20071112	21:37	21:26	22:21	symH
20090624	09:45	09:51	11:02	symH
20120121*3	03:49	04:00	05:02	symH
20120222*2	01:34	01:24	02:16	symH
20120520	01:44	01:37	02:15	symH
20120912	20:17	20:04	21:05	symH
20121126	04:32	04:36	05:14	symH
20150325	09:21	09:06	09:58	symH
20200630	01:35	01:23	02:17	symH
20220615	04:07	04:00	04:35	symH
19991113	12:04	12:13	12:55	weak
20010802	14:27	14:06	15:11	weak
20020315	18:00	18:26	19:21	weak
20030703	13:16	13:09	13:53	weak
20041211	13:03	12:57	13:40	weak
20050131	09:58	09:50	10:22	weak
20110623	02:18	02:24	02:59	weak
20130903	17:02	16:46	17:45	weak
20140810	21:39	21:26	22:31	weak
20141228*2	22:02	22:08	22:57	weak
20150201*3	06:10	06:01	06:39	weak
20150223	22:01	21:49	22:47	weak
20171217	06:36	06:33	07:24	weak
20190404	13:06	13:08	14:09	weak

*1: Identification of geomagnetic SC by both methods (=2), by only SYM-H (=1), and weak/unclear SC (=?)
*2: Reverse shock
*3: Density measurement is skeptical.

Table A3 Timing of IP detection and geomagnetic SC for very oblique 97 samples

Date	SOHO	ACE	SYM-H	SC[*1]
19980503	17:05	17:00	17:44	both
19980508	09:23	09:21	09:52	both
19980613	18:25	18:55	19:26	both
19990416	10:46	10:35	11:26	both
19990702	00:22	00:24	01:00	both
19990712	01:09	01:15	02:20	both
19990912	03:14	03:20	04:00	both
20000205	15:00	14:48	15:44	both
20000608	08:42	08:41	09:10	both
20000710	05:55	05:57	06:39	both
20001126	11:25	11:23	11:58	both
20010131	07:35	07:22	08:05	both
20010411	13:02	13:14	13:44	both
20010413	07:05	07:13	07:35	both
20010618	01:53	01:55	03:00	both
20010827	19:14	19:19	19:53	both
20020217	01:56	02:09	02:55	both
20020228	03:49	04:03	04:51	both
20020530	01:25	01:32	02:05	both
20020717	15:29	15:26	16:03	both
20021109	17:56	17:54	18:50	both
20030320	04:21	04:20	04:44	both
20030817	13:38	13:41	14:22	both
20031026	18:35	18:31	19:09	both
20040722	09:45	09:54	10:37	both
20040829	09:20	09:17	10:06	both
20041109	09:05	09:14	09:31	both
20050612	06:58	06:51	07:46	both
20050727	18:43	18:49	19:39	both
20060819	10:39	10:50	11:32	both
20061216	17:43	17:22	17:56	both
20070507	07:48	07:25	08:27	both
20070927	10:53	10:54	11:52	both
20071217	02:02	02:04	02:53	both
20080624	19:08	19:18	20:11	both
20081124	22:47	22:48	23:52	both
20090303	04:53	04:51	06:03	both
20091021	23:25	23:07	24:18	both
20110310	05:45	06:08	06:34	both
20110610[*3]	08:11	08:07	08:48	both
20110617	02:05	02:01	02:40	both
20110804[*3]	21:10	21:04	21:54	both
20110805	17:23	17:21	17:51	both
20120122	05:18	05:15	06:12	both
20120714[*3]	17:28	17:27	18:10	both
20120720	04:00	04:16	04:49	both
20121008	04:31	04:31	05:17	both
20121112	22:08	22:15	23:13	both
20130317	05:34	05:27	06:01	both
20130518[*3]	00:24	00:23	01:11	both
20130524	17:40	17:36	18:11	both
20130531	15:32	15:30	16:19	both
20130709	19:58	19:56	20:53	both
20131213	12:01	12:08	13:24	both
20140109	19:33	19:31	20:10	both
20140325	19:23	19:25	20:04	both
20140607	15:57	16:08	16:53	both
20140702	23:33	23:26	24:43	both
20140911	23:02	22:57	23:45	both
20140912	15:27	15:26	15:54	both
20150621	15:50	15:41	16:45	both
20150622	04:52	04:51	05:45	both
20150622	18:01	17:59	18:33	both
20160118	20:52	20:55	21:58	both
20160414	06:45	06:51	07:37	both
20170527	14:27	14:39	15:34	both
20180215	08:06	07:50	08:37	both
20180309	17:17	17:22	18:07	both
20190924	12:00	12:03	13:11	both
20201210	01:32	01:33	02:10	both
20220313	10:09	10:06	10:47	both
20000424	08:53	08:51	09:26	symH
20010411	15:18	15:27	15:48	symH
20031106	18:56	19:19	19:41	symH
20031207	14:01	13:41	14:18	symH
20060815	16:26	16:24	17:26	symH
20110805	18:33	18:32	19:02	symH
20130718	12:49	12:41	13:32	symH
20131029	09:25	09:34	10:35	symH
20140706	09:51	09:41	11:05	symH
20150302	02:47	02:37	03:18	symH
20150331[*3]	07:40	07:41	08:34	symH
20150624	13:01	12:57	13:28	symH
20151024[*3]	18:39	18:27	18:56	symH
20211031	09:34	09:29	10:12	symH
19980504	02:36	02:29	02:57	weak
20010830	13:26	13:30	14:12	weak
20020826	10:19	10:46	11:32	weak
20020907	15:53	16:09	16:37	weak
20050325[*2]	16:41	16:37	17:16	weak
20060413	11:41	11:12	12:04	weak
20111112	05:10	05:18	06:00	weak
20120102	00:44	00:59	01:52	weak
20120503	00:59	01:16	02:19	weak
20130602[*2]	01:57	02:10	02:26	weak
20170520[*2]	08:49	08:49	09:23	weak
20210424	22:16	22:22	23:05	weak

*1: Identification of geomagnetic SC by both methods (=2), by only SYM-H (=1), and weak/unclear SC (=?)

*2: Reverse shock

*3: Density measurement is skeptical.

Table A4 Timing of IP detection and geomagnetic SC for SOHO-only 63 samples

Date	**SOHO**	**SYM-H**	**SC**[*1]
19960408	12:33	13:35	both
19970110	00:21	01:05	both
19970209	12:42	13:22	both
19970515[*3]	00:55	02:00	both
19970902	22:03	23:00	both
19971001	00:19	00:59	both
19971023	07:01	08:06	both
19971024	10:19	11:16	both
19971106	22:06	22:49	both
19971122	08:54	09:50	both
19971210	04:22	05:27	both
19971230	01:17	02:10	both
19980106	13:18	14:17	both
19980124	04:48	05:30	both
20000714	15:05	15:32	both
20000715	14:18	14:37	both
20001110	06:00	06:27	both
20010925[*3]	19:51	20:25	both
20011106[*3]	01:20	01:52	both
20011124	05:33	05:55	both
20040106	19:24	19:51	both
20050515	02:19	02:38	both
20050713	04:27	05:13	both
20050717[*3]	01:23	01:36	both
20050911	00:49	01:14	both
20110925	11:12	11:46	both
20120124[*2]	14:33	15:04	both
20120308[*3]	10:53	11:04	both
20130822	18:41	19:26	both
20141101	06:20	07:06	both
19960206	19:02	19:50	symH
19970111	04:27	05:16	symH
19970520	04:46	06:02	symH
19970903	08:11	08:56	symH
19971109	21:51	22:54	symH
19990628	02:28	02:59	symH
20000917	15:19	16:00	symH
20010118	09:18	10:12	symH
20030217	22:55	23:26	symH
20040122[*2]	08:45	09:22	symH
20040126	18:34	19:21	symH
20050429	15:31	16:06	symH
20050529	20:51	21:29	symH
20081028	19:44	20:10	symH
20160311	04:45	05:34	symH
20160725	01:15	02:12	symH
20220519	13:31	13:56	symH
19980131	15:56	16:44	weak
19980325	15:33	16:33	weak
19991204	00:47	01:31	weak
20000427	20:01	21:06	weak
20020326[*2]	10:13	10:50	weak
20030127	16:35	16:59	weak
20030311	15:46	17:16	weak
20030714	10:42	11:18	weak
20030726	12:36	13:06	weak
20031122	09:59	10:29	weak
20050508[*3]	09:07	09:34	weak
20061208	04:11	04:36	weak
20100908	01:07	02:18	weak
20150206	07:40	08:02	weak
20160311[*2]	19:18	19:47	weak
20201023	16:03	16:51	weak

*1: Identification of geomagnetic SC by both methods (=2), by only SYM-H (=1), and weak/unclear SC (=?)
*2: Reverse shock
*3: Density measurement is skeptical.